# Structural and electrical properties of high-performance vanadium dioxide thin layers obtained by reactive magnetron sputtering

Eduard-Nicolae Sirjita, Alexandre Boulle, Jean-Christophe Orlianges, Richard Mayet, Aurelian Crunteanu

# Structural and electrical properties of high-performance vanadium dioxide thin layers obtained by reactive magnetron sputtering

Eduard-Nicolae Sirjita[a,b,*], Alexandre Boulle[b], Jean-Christophe Orlianges[a], Richard Mayet[b], Aurelian Crunteanu[a]

[a] XLIM Research Institute, CNRS/ University of Limoges, 123 Av. Albert Thomas, 87060 Limoges, France;

[b] Institut de Recherche sur les Céramiques (IRCER), CNRS UMR 7315, University of Limoges, Centre Européen de la Céramique, 12 rue Atlantis, Limoges, 87068, France

*Corresponding author: eduard.sirjita@xlim.fr, 123 Av. Albert Thomas, 87060 Limoges, France;

Abstract

Epitaxial vanadium dioxide ($VO_2$) films exhibiting an abrupt metal-insulator transition with resistivity ratios of five orders of magnitude have been grown on (001)-oriented sapphire substrates by reactive magnetron sputtering. The influence of deposition and annealing temperature on the structure and morphology of the layers are discussed as well as their impact on the films' electrical properties. Thus, the $VO_2$ layers obtained using the optimal experimental conditions have electrical resistivity ratios over $10^5$ and can be obtained on substrates as large as three-inch in diameter. The combination of the scalability of magnetron sputtering and the high quality of the films enables the large-scale industrial applications of high quality $VO_2$ layers.

Keywords: Vanadium Dioxide, Reactive magnetron sputtering, Metal-insulator transition

## 1. Introduction

Vanadium Dioxide ($VO_2$) is a well-known electron-correlated material that undergoes a reversible metal to insulator transition (MIT) as well as a structural phase transition (SPT) at a critical temperature ($T_c$), of 67°C (340 K) [1]. During the SPT, the material's crystallographic structure changes from the insulator monoclinic M1 phase at temperatures lower than $T_c$, to a metallic rutile-type R phase, at temperatures higher than $T_c$. The transition is volatile, meaning that $VO_2$ remains in the metallic phase as long as the temperature is higher than $T_c$ and transitions back to the insulator state upon cooling down. Because there is a slight offset of the transition temperature between the heating and the cooling steps, the shape of the transition takes the form of a typical hysteresis curve. Along with the change in the electrical resistivity, the optical characteristics of $VO_2$ change as well, with a transmittance abruptly dropping when reaching the metallic state [2]. In addition to the thermal activation, the phase transition in $VO_2$ films can be triggered by optical [3], mechanical [4], and electrical [5] excitations, making the integration of the material very attractive for applications like Mott memories [6], field-effect transistors [7], micro- and nano-scale oscillators [8–10], sensors [4], high-speed RF-microwave

switches [11,12], THz devices [13,14], or optical switches [15]. The large scale and successful integration of $VO_2$ for most of these applications require good control of the MIT characteristics (either electrical or optical) in one or more of its specific parameters: transition speed, magnitude, hysteresis width, and transition temperature value. These parameters can also be modified by doping the vanadium with metal atoms such as tungsten [16], magnesium [17], molybdenum [18], chromium [19], niobium [20] which results in a modulation of the $T_c$ or a modification in a controlled way of the electrical or optical hysteresis shape. Thus, the material's properties can be adapted to a specific domain of applications requiring lower or higher transition temperatures, a precise hysteresis width, or particular electrical/optical properties in a specific state. Besides the transition temperature and the hysteresis shape, the magnitude of the electrical resistivity change between the two states (also referred to as the resistivity ratio) is critical to a large number of applications [21].

As often reviewed in the literature, the macroscopic electrical and optical performances of $VO_2$ thin films are highly affected by their structural, chemical, and morphological characteristics, which are highly dependent on the experimental parameters of the deposition process [22]. It is also observed that the electrical resistivity ratio can be as high as $10^3$ and even $10^5$ in some instances, although 5 orders of magnitude in a $VO_2$ electrical transition is rarely reported [23,24]. The methods employed for obtaining high-quality thin $VO_2$ films include pulsed laser deposition [25], magnetron sputtering [26], or e-beam evaporation [27,28], as well as chemical methods such as sol-gel deposition [29,30]. Among these methods, magnetron sputtering has the advantages of being a very reproducible method resulting in good uniformity and large-area film depositions, and it is easily scaled up for industry-oriented applications. High-quality $VO_2$ films in terms of crystalline structure, resistivity ratios, large area deposition, and phase transition reliability, are prerequisites for the material integration in high technology readiness level (TRL), commercial-grade devices for electronic and optical communication or sensing applications.

In this paper, we investigate the influence of the synthesis parameters on the structural properties directly influencing the electrical performances of $VO_2$ layers obtained on c-cut sapphire substrates by reactive DC magnetron sputtering. We demonstrate that under specific deposition and annealing conditions, the obtained $VO_2$ layers exhibit highly reproducible and stable resistivity variations of more than five orders of magnitude between the insulating and metallic states. Usually, in magnetron sputtering experiments, the films are obtained in sub-stoichiometric vanadate phases (or phase mixtures, including $VO_2$) with poorer electrical performances and lower crystalline quality which often need long-time annealing processes in order to enhance their electrical and optical properties [31,32].We are showing that, in our experimental conditions, the as-obtained layers have structural and electrical characteristics similar to the $V_2O_3$ phase that can be conveniently transformed into the $VO_2$ phase through an oxygen annealing step. Annealing studies of these as-grown, sub-stoichiometric $V_xO_y$ films such as $V_2O_3$, films were rarely reported, but they are known to show better results in terms of MIT characteristics than as-deposited phase mixtures integrating $VO_2$ [33].

## 2. Experimental details

The $VO_2$ layers were typically obtained on 10 × 10 $mm^2$ c-cut sapphire substrates inside a high-vacuum chamber at an initial base pressure of around $10^{-6}$ Pa using reactive DC magnetron sputtering with a deposition power of 150 W. Alternatively, the films obtained on two-inch and three-inch sapphire wafers showed identical structural and electrical properties as the layers obtained on smaller size substrates. The metallic vanadium target (100-mm diameter of 99.5% quality) was placed at 20 cm from the rotating substrate holder in an upward configuration. The deposition process took place in a reactive Ar and $O_2$ mixture atmosphere. The Ar and $O_2$ flows were independently controlled at flows of 70 sccm for Ar and 2.5 sccm for $O_2$ with the total deposition pressure kept at 0.53 Pa (corresponding to an oxygen partial pressure of 0.018 Pa or 3.4% of the total pressure). Except stated otherwise in the article, the substrate temperature was fixed at 500°C during deposition process, which lasted 30 minutes. After the deposition process, the films were subjected to an *in-situ* annealing step in a pure $O_2$ atmosphere with a flow of 20 sccm in order to improve the stoichiometry of the films. Heating rate of the films were 150°C/min and the annealing took place at different temperatures (450, 550 and 650°C) for 30 minutes, afterwards they were left to cool naturally down to 300°C in oxygen atmosphere and from 300°C to room temperature in vacuum, for a total time of one hour. Within these experimental conditions, the average deposition rate evaluated across the different samples obtained at an $O_2$ flow rate of 2.5 sccm (3.4% partial pressure) was 7.5 nm/min.

The electrical properties of the vanadium oxide films were evaluated in the 25-95°C temperature domain using a four-point probes set-up (four in-line spring-loaded probes with a spacing of 1mm connected to a Keithley 2612B sourcemeter). The heating and cooling of the samples were controlled with a Peltier thermoelectric element and monitored by a Pt100 thermo-couple. Additionally, multiple temperature cycling measurements of the layer's surface resistance were performed using two-probes electrical measurements inside in a Linkam LTS350 temperature controlled stage with controlled heating-cooling ramps and resolutions of 0.1°C.

X-ray diffraction (XRD) measurements were conducted on a Bruker D8 "Discover" X-ray diffractometer. The x-ray beam delivered from a copper target was collimated with a parabolic multilayer mirror and a 2-reflections Ge (220) monochromator tuned to select the $K_{\alpha 1}$ radiation of Cu. The diffracted x-rays were collected using a 1D position sensitive detector ("Lynx Eye") covering a 2 degrees 2θ range with a 0.01° 2θ resolution. The orientation of the film with the substrate in the direction normal to the surface was determined using θ-2θ scans, while the in-plane orientation was determined by conducting φ-scans. Rocking curves were also recorded in order to qualitatively assess the quality of the films. Finally, the samples could be heated to monitor the SPT *in-situ* using an Anton Paar DHS 1100 heating stage. Typical θ-2θ and φ-scans (recorded from the (220) planes of $VO_2$) are displayed in Figure 1. The θ-2θ scan only exhibits the 020 and 040 reflections of $VO_2$ on the one hand, and the 006 and 0012 reflections of sapphire on the other hand, which demonstrates that the (010) planes of $VO_2$ are parallel to the (001) planes of sapphire. The rocking curve corresponding to the (020) lattice planes of $VO_2$ is provided and discussed in section 3.2. In the in-plane direction, we observe a sixfold symmetry instead of the twofold symmetry expected for the (220) planes. This discrepancy is well known and is due to the existence of three structurally equivalent orientations of the (010) planes with respect to the (001) plane of sapphire, hence giving rise to three in-plane epitaxial variants. The corresponding epitaxial relationships read: $[100]_{VO2} \| [210]_{Al2O3}$ ,$[100]_{VO2} \| [-110]_{Al2O3}$ and

$[100]_{VO2}$ ||$[120]_{Al2O3}$. We also notice that the (220) peaks from $VO_2$ are split with peaks appearing at approximately ±2.6° from the central position. This is due to angle mismatch between the β angle of $VO_2$ (122.6°) and the γ angle of $Al_2O_3$ (120°), as already observed in this system [34]. It should be noted that other structural probes allow to determine the epitaxial relationships between a film and a substrate. Among those, transmission electron microscopy which has the advantage of providing real space images of the interface. We here preferred to use XRD because of its non-destructive character and its ability to provide statistically relevant results over macroscopic dimensions of the samples, which is of primary importance for large samples as those considered in this work.

The morphology of the layers was analyzed using a Dimension Icon AFM-Bruker microscope. Raman spectroscopy measurements have been performed using a Raman inverted microscope (Horiba LabRAM HR Evolution) using the excitation from a continuous HeNe laser (λ= 632.8 nm) with an incident power of 6 mW and focused on the sample with a 60× objective to a spot of ~ 2 µm in diameter. As above, a Peltier thermoelectric element was used to control the heating/cooling of the samples.

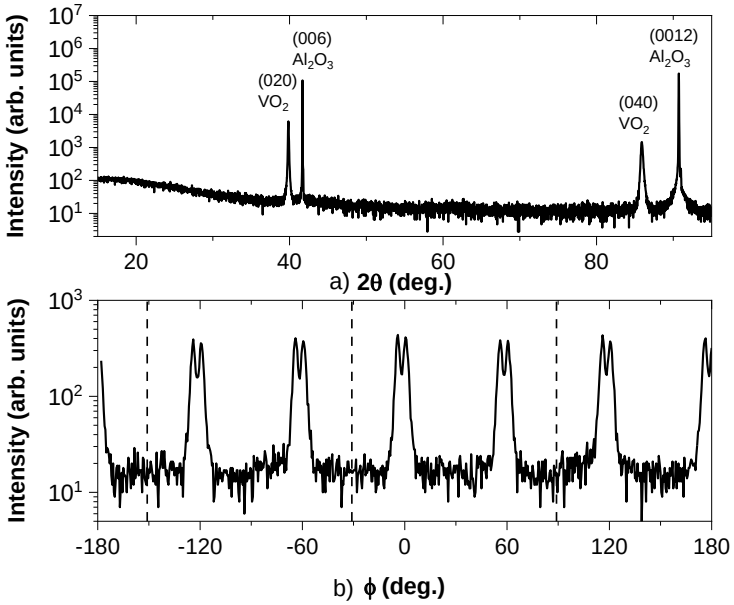


Figure 1. a) θ-2θ scan of a film deposited at 500°C and annealed at 550°C b) typical ϕ-scan recorded for the (220) planes of $VO_2$. The dotted lines indicate the position of the (104) peaks of sapphire.

## 3. Results & Discussion

In order to obtain high-quality films with a large resistivity ratio between the insulator and metallic states, we conducted a systematic investigation of the experimental deposition parameters directly influencing the films' structural and electrical performances.

### 3.1. Film growth

The stability range of vanadium dioxide in the V-O phase diagram is fairly narrow [35], implying very steep experimental conditions for the Ar:$O_2$ ratios in the reactive atmosphere in

order to obtain the desired $VO_2$ stoichiometry. As such, the first step was determining the correct oxygen flow by establishing the target poisoning curve, *i.e.* the evolution of the vanadium target's oxidation state with increasing oxygen flow (Figure 2) that is related to the evolution of the discharged plasma voltage as a function of the specific $O_2$ concentration in the $Ar:O_2$ mixture [36].

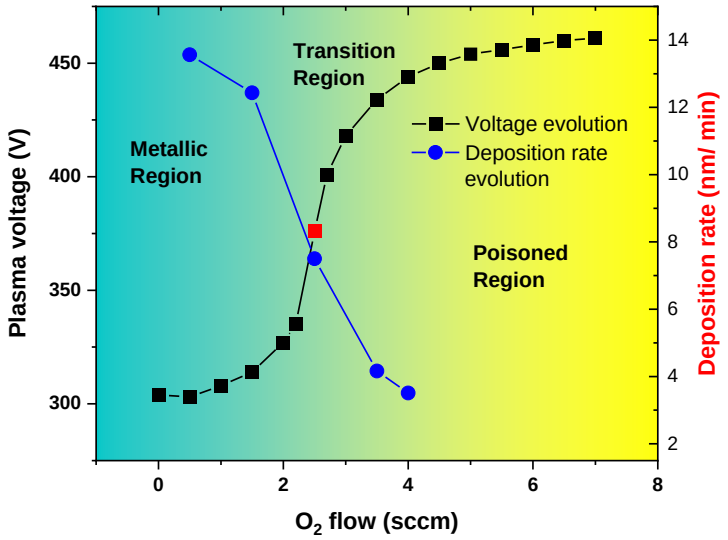


Figure 2. Evolution of plasma voltage and deposition rate during vanadium target sputtering for different oxygen flows. Indicated in red is the operation point for obtaining stoichiometric $VO_2$ films in our experiments (lines between the operating points are eye-guidance only).

During reactive DC magnetron sputtering the evolution of the plasma voltage with the oxygen flow is nonlinear, creating the aforementioned poisoning curve and defining three distinct areas that describe the state of the target (Figure 2). For low oxygen flows, the target operates in a metallic mode, where the oxide formation on the target is lower than the sputtering rate of metallic vanadium, while for high oxygen flows ("poisoned region" in Figure 2), the rate of oxide formation at the target surface is much higher than the sputtering process, leading to the formation of over oxidized films on the substrate. In between these areas, the transition region leads to optimum oxygen incorporation in the obtained films and is characterized by a very steep change of the plasma voltage which can be controlled in some systems through various methods [36]. Since the deposition rate varies inversely proportional with the oxidation state of the target [37], the oxygen flow was fixed at a value (indicated in red in Figure 2) that allows both for enough oxygen incorporation and a high sputtering yield. However, even though the films were deposited in a reactive atmosphere, adapted for optimal oxygen incorporation, the obtained films are still displaying an oxygen-deficient metallic phase. A post-annealing process was therefore required to get the correct V/O stoichiometry in the films.

Three distinct annealing temperatures, of 450, 550, 650°C were chosen to better assess the impact of the annealing process on the films' structural quality. The results are discussed in the following section.

3.2. Effect of post-deposition annealing

The evolution of the θ-2θ XRD scans for films annealed at different temperatures is shown in Figure 3 a). The peak located at 41.678° is the 006 reflection from the sapphire substrate. The peaks observed in the lower angle range can be attributed to the films. The as-deposited film exhibits a single peak that can be attributed to the 006 reflection of $V_2O_3$. For a 450°C annealing temperature, both the $V_2O_3$ and $VO_2$ phases co-exist, as revealed by the appearance of the 020 peak of $VO_2$. A further increase to 550°C annealing temperature fully oxides the film and only the $VO_2$ phase is present. At an even higher annealing temperature of 650°C, no differences can be seen in the θ-2θ scans. Figure 3 b) shows the ω scans around the (020) $VO_2$ reflection of the films annealed at the different temperatures. At 450°C annealing the rocking curve exhibits a broad peak, with full-width at half-maximum FWHM = 0.8°, indicative of a high level of disorder. Upon annealing at 550°C a narrow peak appears in the center of the rocking curve (more visible on the 650°C data) together with a significant narrowing of the broader peak (FWHM = 0.26°). The presence of two-component peak profiles (with a narrow, coherent scattering peak superimposed on a broad, diffuse scattering) is frequently observed in epitaxial thin films. For a review on that topic and a detailed theoretical description see [38].In short, the presence of a coherent peak is due to the development of long range order, *i.e.* enhanced crystalline quality, whereas the broad peak is due to partially correlated disorder (in the present case, rotational disorder, i.e. mosaicity). Finally, at 650°C, although the coherent peak is still visible, the diffuse peaks is widening (FWHM = 0.9°) indicating an increased mosaicity, probably due to the development of defect-induced strains upon grain growth, as discussed below. The 550°C temperature hence appears as an optimum annealing temperature.

$V_2O_3$ and $VO_2$ are the two end-members of the so-called Magnéli phases, $V_nO_{2n-1}$, which only differ by minute variations in the oxygen content that are compensated by crystallographic shears of [$VO_6$] octahedra layers [39,40]. One can therefore transition from $V_2O_3$ to $VO_2$ continuously upon oxygen enrichment, as also observed elsewhere [41]. Moreover, the partial transformation of the films at 450°C has already been noticed [42], although in our case no intermediary vanadium oxide phase was observed in XRD measurements.

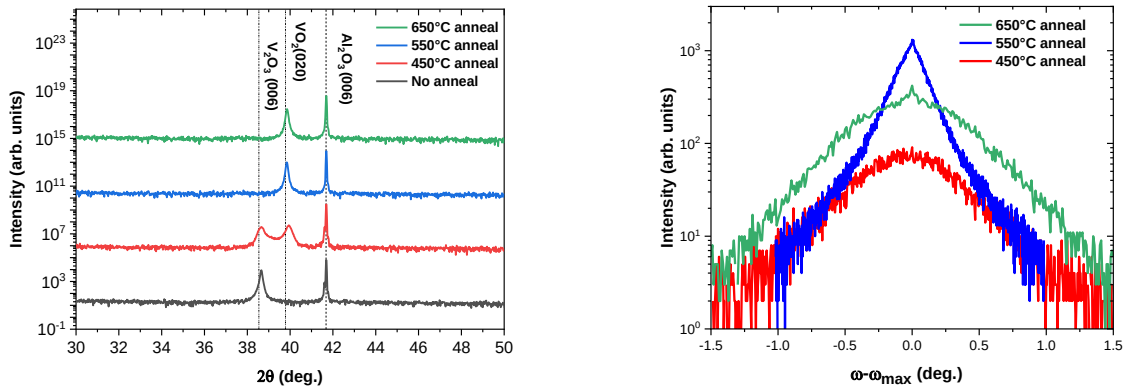


Figure 3. a) θ-2θ scans of as-deposited films at 500°C and the influence of a post-annealing step at different temperatures (450°C, 550°C, 650°C) b) ω scans of films annealed at different temperatures

The four-point probes electrical measurements (Figure 4 a)) reveal that while both the as-deposited and 450°C annealed films are metallic, with the latter having a very low, 0.3 orders of

magnitude transition due to the coexistence of the $VO_2$ and $V_2O_3$ phases, for higher annealing temperatures (550°C and 650°C), the obtained films show a high, five orders of magnitude change from the room temperature (RT) insulator phase ($\rho = 1.5\times10^6$ Ω·cm) to the high-temperature metallic phase ($\rho$ = 11.2 Ω·cm), with almost identical resistivity curves. It is worth mentioning that the transition width is slightly higher for the film annealing at the highest temperature, possibly due to an increase of structural defects as observed in the rocking curves, and further discussed below. The metal insulator transition is accompanied by the M1-R structural phase transition as attested by the temperature-resolved XRD measurement shown in Figure 5. The measurements were recorded in the range of 44°C-90°C for a typical $VO_2$ film (deposited at 500°C and annealed at 550°C). The 2D diffraction angles-temperature intensity mapping in Figure 5 show a clear phase transition from the low-temperature monoclinic M1 $VO_2$ phase to the rutile R one, this last one being stabilized for temperature higher than 68°C.

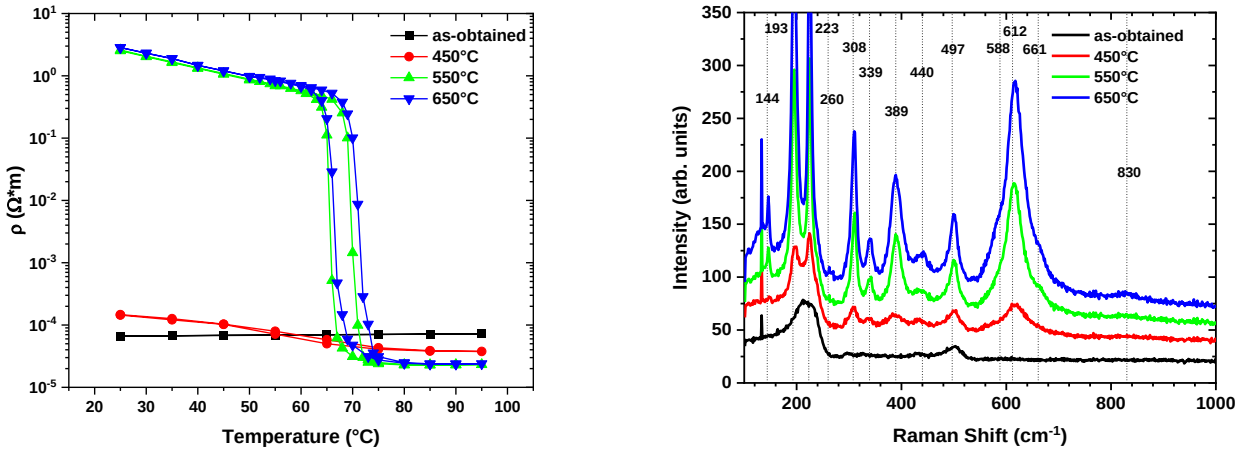


Figure 4. a) Hysteresis curves of the electrical sheet resistance evolution with temperature increase for $VO_2$ films annealed at different temperatures. b) Raman scattering results for $VO_2$ films annealed at different temperatures

Raman spectroscopy measurements (Figure 4 b)) show that all the investigated films, except the as-deposited ones (without the annealing step), present similar vibrational modes typical to $VO_2$ films [43]. We have identified a total of 13 peaks for the $VO_2$ phase. Thus, the peaks at ~144, 193, 223, 260, 308, 339, 389, 440, 497, 588, 612, 661 and 830 $cm^{-1}$ are typical of the $VO_2$ M1 phase [43,44]. All of the peaks, except the ones at 193 and 223 which are related to the lattice motion involving V-V bonds, were assigned to vibrational modes of V-O bonds [43]. The wide peak at around ~220 $cm^{-1}$ on the Raman spectra corresponding to the non-annealed sample (black, lowest curve on Figure 4 b)) corresponds to an overlap of an $A_{1g}$ and an $E_g$ symmetry modes, and, associated with the peak at ~500 $cm^{-1}$ related to the $A_{1g}$ phonon mode, are indicative of the $V_2O_3$ phase [45], confirming the XRD analysis. The lower peak intensities of the 450°C-annealed sample could be due to the under-oxidation and phase mixing.

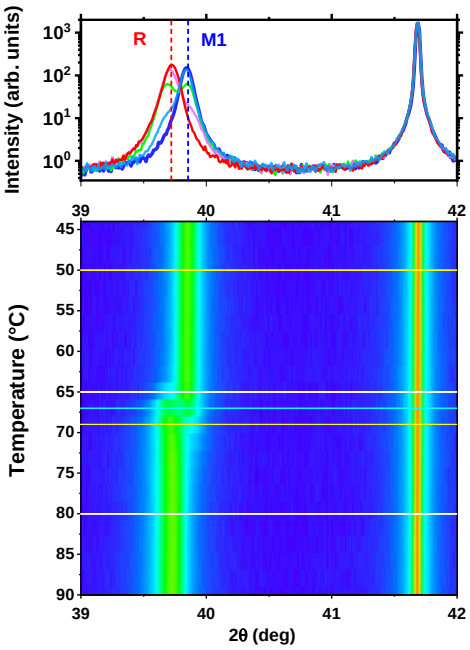


Figure 5. XRD intensity- temperature mapping and extracted θ-2θ scans showing the M1-to-R phase evolution of the (020) peak of $VO_2$ with increasing temperature

### 3.3. Effect of deposition temperature

In addition to the annealing temperature we also investigated the effect of deposition temperature, while keeping a constant 550°C annealing temperature. The XRD results for deposition temperatures RT, 150, 400, 500 and 600°C are shown in Figure 6. Deposition performed at 400°C and higher show a single oriented $VO_2$ phase. For depositions at room temperature a phase mixture is observed (despite the post deposition annealing). In the case of films obtained at 150°C, only the M1 phase of $VO_2$ is present, but the XRD θ-2θ scans reveal two peaks, one corresponding to the (011) lattice planes and the other to the (020) lattice planes. Even if the (011) orientation has been noticed in films with a high level of strain, additional investigations need to be done in order to draw a clear correlation between this orientation and the strain developed in the films [46]. Grazing incidence XRD scans (not shown here) performed on the room temperature and 150°C deposited thin films reveal that all peaks of $VO_2$ are present, *i.e.* the films are largely polycrystalline. Conversely, no peaks are detected in the grazing incidence scans corresponding to samples annealed at 400°C and above, confirming the complete epitaxial nature of the films.

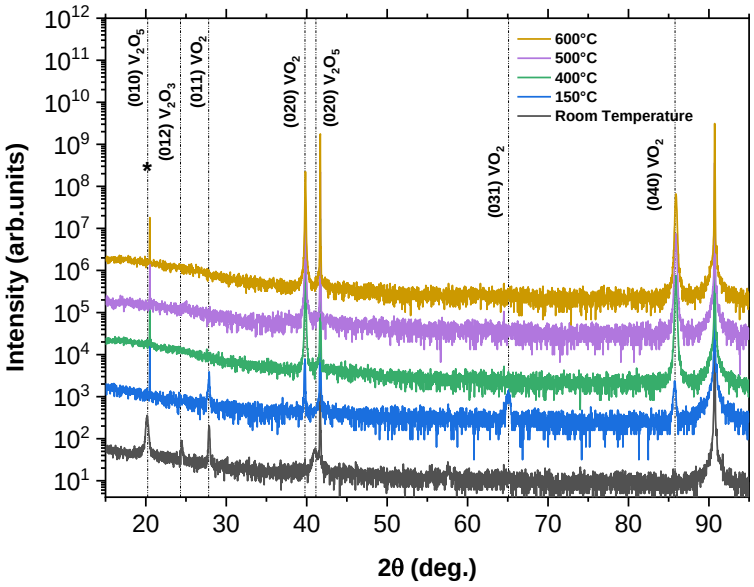


Figure 6. θ-2θ scans of films fabricated at RT, 150, 400, 500 and 600 °C and annealed at 550°C (the peak labeled "*" is the forbidden 003 reflection of $Al_2O_3$ which is excited by multiple diffraction in the high quality $Al_2O_3$ crystals.)

The associated four-point probes electrical measurements of the samples obtained at different deposition temperatures are shown in Figure 7. They are clearly showing that the increase of the temperature during deposition (while keeping the annealing temperature constant at 550°C) not only improves the crystallinity of the samples, as evidenced by XRD, but also results in increasing their electrical resistivity ratios by one order of magnitude. Thus, the sample obtained at RT shows ratios of $10^4$ (from $\rho = 2.28\times10^6$ Ω·cm to $\rho = 1.56\times10^2$ Ω·cm) while the ones obtained at deposition temperatures higher than 500°C present electrical resistivity ratios higher than $10^5$ (as mentioned in the annealing section discussions), which are among the highest currently reported in literature.

The resistivity curves for all deposition temperatures higher than 150°C superimpose perfectly, which shows the reproducibility and the stability of the deposition process.

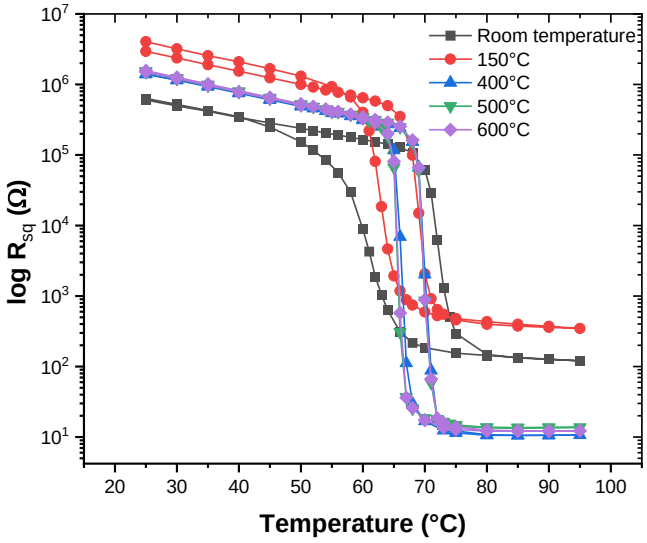


Figure 7. Electrical hysteresis curve of sheet resistance ($R_{sq}$) with temperature evolution for $VO_2$ films deposited at different temperatures

## 3.4. Discussion

In order to get more insight into the electrical resistivity data, we extracted the following parameters from the resistivity *vs.* temperature curves: (i) the hysteresis width (ΔH), given by the difference between the peaks of the first derivatives of log(resistivity) versus temperature, (ii) the transition width (or transition spread, ΔT), given by the difference between the peaks of the second derivatives, and (iii) the MIT temperature, $T_{MIT}$, calculated by averaging the temperature peaks of the first derivative (*i.e.* the heating, $T_{up}$, and cooling, $T_{down}$, transition temperatures). Differentiating experimental (stepped and noisy) data leads to wild oscillations in the derivatives which prevents any reliable analysis. To overcome this issue the data was interpolated and smoothed before taking the derivative (see Figure 8).

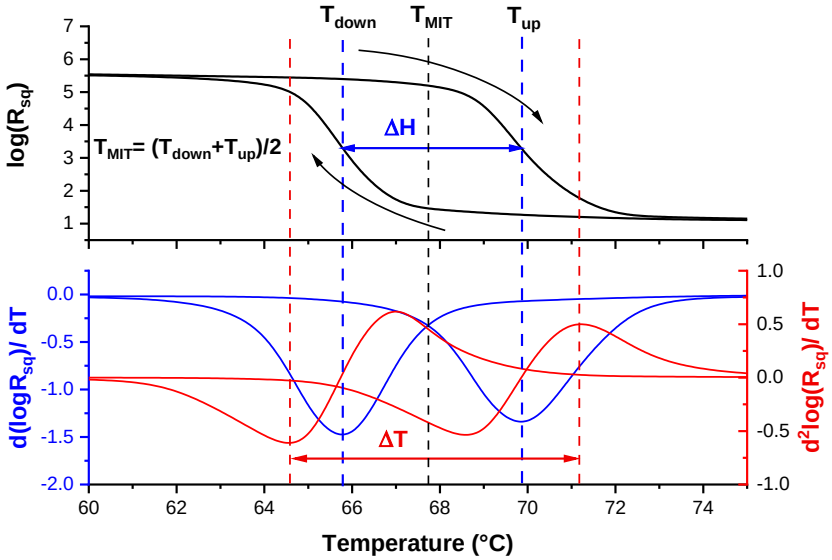


Figure 8. Sheet resistance hysteresis curve and associated 1st and 2nd order derivative of a typical high-quality $VO_2$ sample (deposited at 500°C and annealed at 550°C) allowing to extract the MIT transition temperature, hysteresis and transition widths (black line - interpolated and smoothed experimental curve).

The evolution of these parameters reported in Table 1 indicates that when the deposition temperature is increasing from RT to 600°C (for identical annealing temperatures of 550°C), both the hysteresis and transition widths are decreasing from 10.7° and 15°C down to values as low as 4° and 5°C, respectively. At the same time, the $T_{MIT}$ at which the MIT occurs is stabilizing at values close to the theoretical 67°C. AFM measurements (Figure 9) reveal that for higher deposition temperatures the roughness of the layers is decreasing (from 9.8 nm for RT deposition to 8.9 nm for 500°C deposition temperature) while the average grain size is increasing (from 145 nm at RT deposition to 207 nm at 500°C deposition).

Table 1. Hysteresis curves parameters from samples deposited at different temperatures

| Deposition temperature (°C) | Annealing temperature (°C) | Hysteresis width (°C) | Transition width (°C) | $T_{MIT}$ (°C) | Electrical switch ratio |
|---|---|---|---|---|---|
| RT | 550 | 10.7 | 15 | 66.6 | $1.7\times10^4$ |
| 150 | 550 | 6.3 | 8.0 | 65.9 | $1.4\times10^4$ |
| 400 | 550 | 3.5 | 6.0 | 68.0 | $1.7\times10^5$ |
| 500 | 550 | 4.0 | 5.2 | 67.6 | $1.3\times10^5$ |
| 600 | 550 | 4.0 | 5.0 | 67.6 | $1.5\times10^5$ |
| 500 | 650 | 4.9 | 6.0 | 68.8 | $1.4\times10^5$ |

The values of the transition spread and hysteresis width are controlled by the density of defects and the crystalline nature of the films [24,47]. A higher density of defects (vacancies, clusters, impurities, grain boundaries, etc.) will decrease the amplitude of the transition and affect the

ΔH and ΔT: the transition width is proportional to the density of defects while the hysteresis width is also related to the grain size. In our case, as the films' quality increases with the deposition temperature and the grains are growing, *i.e.* the defects associated with grain boundaries lessen and so does the transition width. It can nonetheless be observed that for films deposited at a fixed 550°C temperature, increasing the annealing temperature from 550°C to 650°C slightly degrades the MIT parameters with a hysteresis width and transition width increasing from 4° and 5.2° to 4.9° and 6°. This is consistent with the rocking curve data discussed in section 3.2.

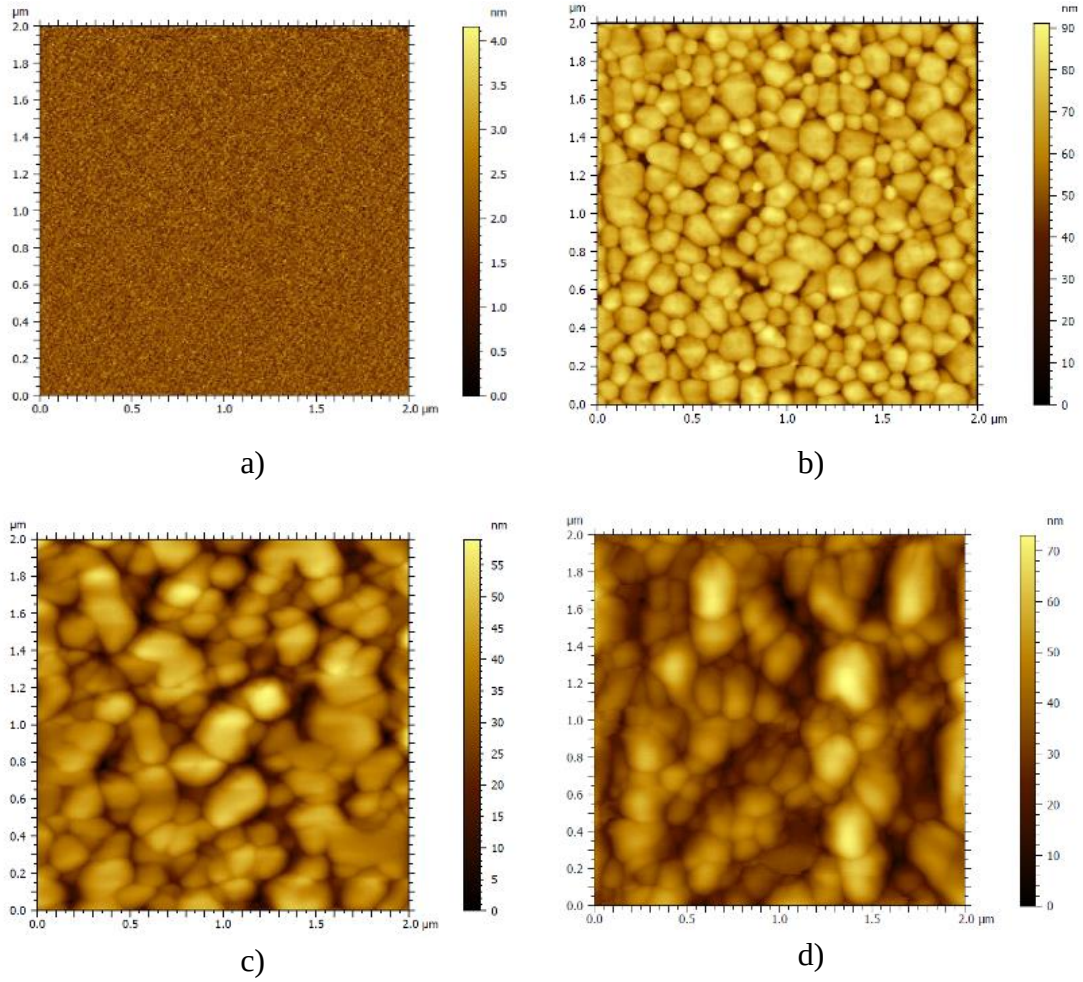


Figure 9. Atomic force microscopy analysis of a) an as-obtained sample at 500°C showing roughness of Sq – 0.5 nm b) of a film obtained at RT and annealed at 500°C (Sq – 9.8 nm, average grain length – 145 nm), c) a layer obtained at 500°C and annealed at 550°C (Sq – 8.94, average grain length – 207 nm) and d) a film obtained at 500°C and annealed at 650°C (Sq – 11.2 nm, average grain size – 218 nm)

In order to test the stability in time that would reflect systematic use of the $VO_2$ layers, we have applied repeated thermal heating-cooling cycles on a $VO_2$ film obtained in typical conditions (500°C deposition and 550°C annealing temperatures) and measured their electrical resistance using a two-probe configuration. The measurements were performed by periodically ramping up and down the temperature in the 30-100°C range with heating/cooling rates of 10°C/min (25

cycles) and with rates of 20°C/min for more than 60 cycles. Figure 10 shows the evolution of the film's surface resistance with time, and reveals no degradation of the electrical properties of the layer throughout the temperature cycling and an excellent stability for repeated thermal activation between the two states of the $VO_2$.

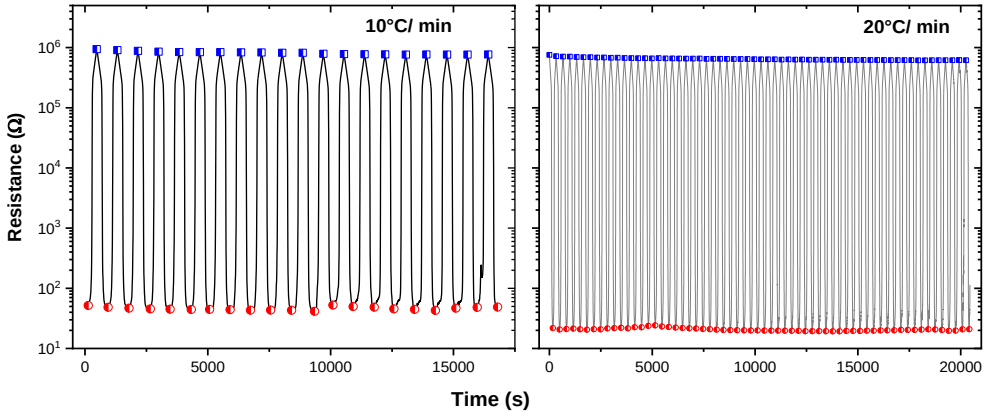


Figure 10. $VO_2$ layer surface resistance evolution with time for multiple thermal cycles with 10°C/min and 20°C/min rates

Table 2 lists our electrical performances results and relevant experimental parameters compared with previously reported $VO_2$ layers fabricated by RF, DC and reactive DC magnetron sputtering techniques. From this data it can be concluded that our films, grown using a rather flexible methodology and convenient deposition rates, outperform most of the available published reports, in particular in terms of the electrical MIT magnitude.

Table 2. Comparison of relevant experimental parameters and electrical performances of previously reported $VO_2$ films obtained using magnetron sputtering techniques

| **Ref.** | **Deposition method** | **Resistivity change** | **Substrate** | **Target** | **Deposition temp. (°C)** | **Annealing temp. (°C)** | **Annealing time (min)** | **Thickness (nm)** |
|---|---|---|---|---|---|---|---|---|
| [48] | Reactive DC Sputtering | ~$10^3$ | glass | V 99.9% | 500 | No | No | *N.P. |
| [49] | Reactive DC Sputtering | $10^4$ | glass and silicon | V 99.9% | 200-220 | 300 | 30 | 100-150 |
| [50] | DC Sputtering | 3x $10^3$ | c-sapphire | *N.P. | *N.P. | 425 | 240 | 200 |
| [51] | DC Sputtering | 2x $10^4$ | c-sapphire | V 99.9% | *N.P. | 470°C | *N.P. | ~100 |
| [52] | RF Sputtering | 1.19x $10^5$ | c-sapphire | $VO_2$ | 500 | 500 | 40 | 110 |
| [33] | RF Sputtering | $10^4$ | c-sapphire | V 99.9% | 400 | 450 | 40 | 280 |
| **This work** | **Reactive DC Sputtering** | **1.67x $10^5$** | **c-sapphire** | **V 99.5%** | **400** | **550** | **30** | **280** |

*N.P. – Not provided

## 4. Conclusion

High-quality $VO_2$ films were grown on c-cut sapphire substrates by means of reactive magnetron sputtering from a metallic vanadium target under Ar and $O_2$ atmosphere. The as-deposited films exhibit under-oxidized metallic phases requiring an additional post-annealing of 550°C or higher, in order to obtain high-quality films that display electrical resistivity ratios as high as $1.67\times10^5$ between the insulating and metallic states. It was found that besides post-annealing, the gradual increase of the deposition temperature is highly improving the structural and electrical quality of the obtained layers. The $VO_2$ films' electrical characteristics obtained in the optimal experimental conditions are very stable during thermal cycling inducing MIT, which implies that no changes in films' crystalline structure or stoichiometry during cycling. The high electrical performances of the fabricated $VO_2$ films and their stability, combined with the ability of magnetron sputtering to perform large area deposition, hold a strong potential for large-scale $VO_2$ integration in electrical and optical devices.

## Declaration of competing interest

The authors declare that they have no known competing financial interests or personal relationships that could have appeared to influence the work reported in this paper.

## Acknowledgments

This work benefited from government support managed by the National Research Agency under the Investments for the future program with the reference ANR-10-LABX-0074-01 Sigma-LIM. The authors acknowledge support from the PETACom FET Open H2020 grant number 829153 and the Femto-$VO_2$ Project (Nouvelle-Aquitaine region).

References

[1] F.J. Morin, Oxides Which Show a Metal-to-Insulator Transition at the Neel Temperature, Phys. Rev. Lett. 3 (1959) 34–36. https://doi.org/10.1103/PhysRevLett.3.34.

[2] T.D. Vu, Z. Chen, X. Zeng, M. Jiang, S. Liu, Y. Gao, Y. Long, Physical vapour deposition of vanadium dioxide for thermochromic smart window applications, J. Mater. Chem. C. 7 (2019) 2121–2145. https://doi.org/10.1039/C8TC05014G.

[3] A. Cavalleri, Cs. Tóth, C.W. Siders, J.A. Squier, F. Ráksi, P. Forget, J.C. Kieffer, Femtosecond Structural Dynamics in VO 2 during an Ultrafast Solid-Solid Phase Transition, Phys. Rev. Lett. 87 (2001) 237401. https://doi.org/10.1103/PhysRevLett.87.237401.

[4] B. Hu, Y. Ding, W. Chen, D. Kulkarni, Y. Shen, V.V. Tsukruk, Z.L. Wang, External-Strain Induced Insulating Phase Transition in VO2 Nanobeam and Its Application as Flexible Strain Sensor, Adv. Mater. 22 (2010) 5134–5139. https://doi.org/10.1002/adma.201002868.

[5] G. Stefanovich, A. Pergament, D. Stefanovich, Electrical switching and Mott transition in VO $_2$, J. Phys. Condens. Matter. 12 (2000) 8837–8845. https://doi.org/10.1088/0953-8984/12/41/310.

[6] A. Moatti, R. Sachan, J. Narayan, Volatile and non-volatile behavior of metal–insulator transition in $VO_2$ through oxygen vacancies tunability for memory applications, J. Appl. Phys. 128 (2020) 045302. https://doi.org/10.1063/5.0006671.
[7] D. Ruzmetov, G. Gopalakrishnan, C. Ko, V. Narayanamurti, S. Ramanathan, Three-terminal field effect devices utilizing thin film vanadium oxide as the channel layer, J Appl Phys. (2010) 114516. https://doi.org/10.1063/1.3408899.
[8] Md.S. Mian, K. Okimura, J. Sakai, Self-oscillation up to 9 MHz based on voltage triggered switching in $VO_2$ /TiN point contact junctions, J. Appl. Phys. 117 (2015) 215305. https://doi.org/10.1063/1.4922122.
[9] R. Tobe, Md.S. Mian, K. Okimura, Coupled oscillations of $VO_2$ -based layered structures: Experiment and simulation approach, J. Appl. Phys. 127 (2020) 195103. https://doi.org/10.1063/5.0001382.
[10] A. Beaumont, J. Leroy, J.-C. Orlianges, A. Crunteanu, Current-induced electrical self-oscillations across out-of-plane threshold switches based on $VO_2$ layers integrated in crossbars geometry, J. Appl. Phys. 115 (2014) 154502. https://doi.org/10.1063/1.4871543.
[11] J. Jiang, G. Chugunov, R.R. Mansour, Fabrication and characterization of VO2-based series and parallel RF switches, in: 2017 IEEE MTT- Int. Microw. Symp. IMS, IEEE, Honololu, HI, USA, 2017: pp. 278–280. https://doi.org/10.1109/MWSYM.2017.8059096.
[12] A. Mennai, A. Bessaudou, F. Cosset, C. Guines, D. Passerieux, P. Blondy, A. Crunteanu, High cut-off frequency RF switches integrating a metal-insulator transition material, in: 2015 IEEE MTT- Int. Microw. Symp., IEEE, Phoenix, AZ, USA, 2015: pp. 1–3. https://doi.org/10.1109/MWSYM.2015.7166910.
[13] H. Wong, K.X. Wang, L. Huitema, A. Crunteanu, Active meta polarizer for terahertz frequencies, Sci. Rep. 10 (2020) 15382. https://doi.org/10.1038/s41598-020-71990-z.
[14] C. Han, E.P.J. Parrott, G. Humbert, A. Crunteanu, E. Pickwell-MacPherson, Broadband modulation of terahertz waves through electrically driven hybrid bowtie antenna-VO2 devices, Sci. Rep. 7 (2017) 12725. https://doi.org/10.1038/s41598-017-13085-w.
[15] S.A. Dönges, O. Khatib, B.T. O'Callahan, J.M. Atkin, J.H. Park, D. Cobden, M.B. Raschke, Ultrafast Nanoimaging of the Photoinduced Phase Transition Dynamics in $VO_2$, Nano Lett. 16 (2016) 3029–3035. https://doi.org/10.1021/acs.nanolett.5b05313.
[16] T.D. Manning, I.P. Parkin, M.E. Pemble, D. Sheel, D. Vernardou, Intelligent Window Coatings: Atmospheric Pressure Chemical Vapor Deposition of Tungsten-Doped Vanadium Dioxide, Chem. Mater. 16 (2004) 744–749. https://doi.org/10.1021/cm034905y.
[17] J. Zhou, Y. Gao, X. Liu, Z. Chen, L. Dai, C. Cao, H. Luo, M. Kanahira, C. Sun, L. Yan, Mg-doped VO2 nanoparticles: hydrothermal synthesis, enhanced visible transmittance and decreased metal–insulator transition temperature, Phys. Chem. Chem. Phys. 15 (2013) 7505. https://doi.org/10.1039/c3cp50638j.
[18] T.J. Hanlon, J.A. Coath, M.A. Richardson, Molybdenum-doped vanadium dioxide coatings on glass produced by the aqueous sol–gel method, Thin Solid Films. 436 (2003) 269–272. https://doi.org/10.1016/S0040-6090(03)00602-3.
[19] S. Hong, M. Lee, M.W. Lee, D. Kim, Sharp Phase Transition by the Enhanced Lattice Stability of Low-Temperature Phase of Cr-Doped $VO_2$ , Bull. Korean Chem. Soc. 42 (2021) 1232–1238. https://doi.org/10.1002/bkcs.12353.
[20] S. Guan, M. Souquet-Basiège, O. Toulemonde, D. Denux, N. Penin, M. Gaudon, A. Rougier, Toward Room-Temperature Thermochromism of $VO_2$ by Nb Doping: Magnetic Investigations, Chem. Mater. 31 (2019) 9819–9830. https://doi.org/10.1021/acs.chemmater.9b03906.

[21] Z. Yang, C. Ko, S. Ramanathan, Oxide Electronics Utilizing Ultrafast Metal-Insulator Transitions, Annu. Rev. Mater. Res. 41 (2011) 337–367. https://doi.org/10.1146/annurev-matsci-062910-100347.
[22] C. Liu, Y. Wang, Z. Tian, Y. Mei, Low-dimensional vanadium dioxide nanomaterials: fabrication, properties and applications, J. Phys. Mater. 3 (2020) 032007. https://doi.org/10.1088/2515-7639/aba1d6.
[23] Q. Tricas, P. Besnier, X. Castel, C. Le Paven, P. Foutrel, $VO_2$ Thin Film as a Temperature Activated Electromagnetic Shield, in: 2021 IEEE Int. Jt. EMCSIPI EMC Eur. Symp., IEEE, Raleigh, NC, USA, 2021: pp. 38–43. https://doi.org/10.1109/EMC/SI/PI/EMCEurope52599.2021.9559174.
[24] R. Molaei, R. Bayati, F. Wu, J. Narayan, A microstructural approach toward the effect of thickness on semiconductor-to-metal transition characteristics of $VO_2$ epilayers, J. Appl. Phys. 115 (2014) 164311. https://doi.org/10.1063/1.4872030.
[25] H. Liu, O. Vasquez, V.R. Santiago, L. Diaz, A.J. Rua, F.E. Fernandez, Novel pulsed-laser-deposition—VO2 thin films for ultrafast applications, J. Electron. Mater. 34 (2005) 491–496. https://doi.org/10.1007/s11664-005-0056-y.
[26] P. Guo, Vanadium dioxide phase change thin films produced by thermal oxidation of metallic vanadium, Thin Solid Films. (2020) 6.
[27] V. Théry, A. Boulle, A. Crunteanu, J.C. Orlianges, A. Beaumont, R. Mayet, A. Mennai, F. Cosset, A. Bessaudou, M. Fabert, Structural and electrical properties of large area epitaxial $VO_2$ films grown by electron beam evaporation, J. Appl. Phys. 121 (2017) 055303. https://doi.org/10.1063/1.4975117.
[28] J. Leroy, A. Bessaudou, F. Cosset, A. Crunteanu, Structural, electrical and optical properties of thermochromic VO2 thin films obtained by reactive electron beam evaporation, Thin Solid Films. 520 (2012) 4823–4825. https://doi.org/10.1016/j.tsf.2011.08.035.
[29] Y. Gao, H. Luo, Z. Zhang, L. Kang, Z. Chen, J. Du, M. Kanehira, C. Cao, Nanoceramic VO2 thermochromic smart glass: A review on progress in solution processing, Nano Energy. 1 (2012) 221–246. https://doi.org/10.1016/j.nanoen.2011.12.002.
[30] Z. Fang, S. Tian, B. Li, Q. Liu, B. Liu, X. Zhao, G. Sankar, VO2/ZnO bilayer films with enhanced thermochromic property and durability for smart windows, Appl. Surf. Sci. 540 (2021) 148414. https://doi.org/10.1016/j.apsusc.2020.148414.
[31] S. Chen, H. Zhang, High visible transmittance of VO2 film prepared by DC magnetron sputtering with situ annealing, J. Opt. 50 (2021) 508–511. https://doi.org/10.1007/s12596-021-00719-6.
[32] R.G. Huang, D.P. Zhang, T. Zhang, Y. Li, Y.T. Chen, Y.L. Zhong, P. Fan, Properties of Vanadium Oxide Films Prepared by DC Reactive Magnetron Sputtering at Different Oxygen Partial Pressures, Adv. Mater. Res. 538–541 (2012) 105–109. https://doi.org/10.4028/www.scientific.net/AMR.538-541.105.
[33] K. Okimura, Y. Suzuki, Epitaxial Growth of $V_2O_3$ Thin Films on *c* -Plane $Al_2O_3$ in Reactive Sputtering and Its Transformation to $VO_2$ Films by Post Annealing, Jpn. J. Appl. Phys. 50 (2011) 065803. https://doi.org/10.1143/JJAP.50.065803.
[34] V. Théry, A. Boulle, A. Crunteanu, J.C. Orlianges, A. Beaumont, R. Mayet, A. Mennai, F. Cosset, A. Bessaudou, M. Fabert, Role of thermal strain in the metal-insulator and structural phase transition of epitaxial VO 2 films, Phys. Rev. B. 93 (2016) 184106. https://doi.org/10.1103/PhysRevB.93.184106.
[35] C.H. Griffiths, H.K. Eastwood, Influence of stoichiometry on the metal-semiconductor transition in vanadium dioxide, J. Appl. Phys. 45 (1974) 2201–2206. https://doi.org/10.1063/1.1663568.

[36] K. Strijckmans, R. Schelfhout, D. Depla, Tutorial: Hysteresis during the reactive magnetron sputtering process, J. Appl. Phys. 124 (2018) 241101. https://doi.org/10.1063/1.5042084.
[37] J.T. Gudmundsson, Physics and technology of magnetron sputtering discharges, Plasma Sources Sci. Technol. 29 (2020) 113001. https://doi.org/10.1088/1361-6595/abb7bd.
[38] A. Boulle, R. Guinebretière, A. Dauger, Phenomenological analysis of heterogeneous strain fields in epitaxial thin films using x-ray scattering, J. Phys. Appl. Phys. 38 (2005) 3907–3920. https://doi.org/10.1088/0022-3727/38/21/012.
[39] U. Schwingenschlögl, V. Eyert, U. Eckern, From $VO_2$ to $V_2O_3$: The metal-insulator transition of the Magnéli phase $V_6O_{11}$, Europhys. Lett. EPL. 61 (2003) 361–367. https://doi.org/10.1209/epl/i2003-00182-9.
[40] Q. Zhang, W. Liu, Y. Zhou, J. Li, T. Sun, Q. Liu, Y. Ma, J. Wang, J. Li, R. Zhao, Y. Sui, T. Matsumoto, N. Muroyama, A. Yamano, K.D.M. Harris, Z.J. Shen, O. Terasaki, Andersson-Magnéli Phases $Ti_nO_{2n-1}$: Recent Progress Inspired by Swedish Scientists, Z. Für Anorg. Allg. Chem. 647 (2021) 126–133. https://doi.org/10.1002/zaac.202000408.
[41] B. Hong, J. Zhao, K. Hu, Y. Yang, Z. Luo, X. Li, C. Gao, Facile synthesis of various epitaxial and textured polymorphs of vanadium oxide thin films on the (0006)-surface of sapphire substrates, RSC Adv. 7 (2017) 22341–22346. https://doi.org/10.1039/C7RA00389G.
[42] B. Van Bilzen, P. Homm, L. Dillemans, C.-Y. Su, M. Menghini, M. Sousa, C. Marchiori, L. Zhang, J.W. Seo, J.-P. Locquet, Production of VO2 thin films through post-deposition annealing of V2O3 and VOx films, Thin Solid Films. 591 (2015) 143–148. https://doi.org/10.1016/j.tsf.2015.08.036.
[43] F. Ureña-Begara, A. Crunteanu, J.-P. Raskin, Raman and XPS characterization of vanadium oxide thin films with temperature, Appl. Surf. Sci. 403 (2017) 717–727. https://doi.org/10.1016/j.apsusc.2017.01.160.
[44] M. Pan, J. Liu, H. Zhong, S. Wang, Z. Li, X. Chen, W. Lu, Raman study of the phase transition in VO2 thin films, J. Cryst. Growth. 268 (2004) 178–183. https://doi.org/10.1016/j.jcrysgro.2004.05.005.
[45] P. Shvets, O. Dikaya, K. Maksimova, A. Goikhman, A review of Raman spectroscopy of vanadium oxides, J. Raman Spectrosc. 50 (2019) 1226–1244. https://doi.org/10.1002/jrs.5616.
[46] K. Matsuoka, K. Okimura, N.H. Azhan, M. Zaghrioui, J. Sakai, Persistent M2 phase in strongly strained (011)-oriented grains in $VO_2$ films grown on sapphire (001) in reactive sputtering, J. Appl. Phys. 125 (2019) 165304. https://doi.org/10.1063/1.5068700.
[47] J.Y. Suh, R. Lopez, L.C. Feldman, R.F. Haglund, Semiconductor to metal phase transition in the nucleation and growth of VO2 nanoparticles and thin films, J. Appl. Phys. 96 (2004) 1209–1213. https://doi.org/10.1063/1.1762995.
[48] L. Chotirat, S. Niyomwas, S. Supothina, W. Wongpisan, K. Waree, Synthesis and Electrical Resistance Property of Vanadium Oxide Thin Films by DC Magnetron Sputtering, Mater. Sci. Forum. 998 (2020) 185–190. https://doi.org/10.4028/www.scientific.net/MSF.998.185.
[49] Yu. Goltvyanskyi, I. Khatsevych, A. Kuchuk, V. Kladko, V. Melnik, P. Lytvyn, V. Nikirin, B. Romanyuk, Structural transformation and functional properties of vanadium oxide films after low-temperature annealing, Thin Solid Films. 564 (2014) 179–185. https://doi.org/10.1016/j.tsf.2014.05.067.
[50] S. Yu, S. Wang, M. Lu, L. Zuo, A metal-insulator transition study of $VO_2$ thin films grown on sapphire substrates, J. Appl. Phys. 122 (2017) 235102. https://doi.org/10.1063/1.4997437.

[51] J. Sang, T. Zheng, L. Xu, X. Zhou, S. Tian, J. Sun, X. Xu, J. Wang, S. Zhao, Y. Liu, Modulating the metal-insulator transition in VO2/Al2O3 (001) thin films by grain size and lattice strain, J. Alloys Compd. 876 (2021) 160208. https://doi.org/10.1016/j.jallcom.2021.160208.
[52] D.H. Jung, H.S. So, K.H. Ko, J.W. Park, H. Lee, T.T.T. Nguyen, S. Yoon, Electrical and optical properties of VO2 thin films grown on various sapphire substrates by using RF sputtering deposition, J. Korean Phys. Soc. 69 (2016) 1787–1797. https://doi.org/10.3938/jkps.69.1787.